Geothermics 74 (2018) 226–239

Contents lists available at ScienceDirect

Geothermics

journal homepage: www.elsevier.com/locate/geothermics

Geochemical characterization of the geothermal system at Villarrica volcano, Southern Chile; Part 1: Impacts of lithology on the geothermal reservoir

S. Held[a,*], E. Schill[b], J. Schneider[c], F. Nitschke[a], D. Morata[d,e], T. Neumann[a], T. Kohl[a]

[a] Institute of Applied Geosciences, Karlsruhe Institute of Technology (KIT), Karlsruhe, Germany
[b] Institute for Nuclear Waste Disposal, Karlsruhe Institute of Technology (KIT), Karlsruhe, Germany
[c] Hydrosion GmbH, Munich, Germany
[d] Andean Geothermal Center of Excellence (CEGA), Universidad de Chile, Santiago, Chile
[e] Department of Geology, Facultad de Ciencias Físicas y Matemáticas, Universidad de Chile, Santiago, Chile

ARTICLE INFO

Keywords:
Anthropogenic tracers
Lithology-controlled geothermal system
Medium-enthalpy geothermal resource
Geothermal fluid circulation

ABSTRACT

Besides temperature, mineralogy, residence time and dilution are crucial for assessing water-rock interaction intensity. The geothermal system at the Villarrica-Quetrupillán-Lanín volcanic chain, Southern Chile, is located across a prominent lithological transition from plutonic rocks of the North Patagonian Batholith (NPB) to volcano-sedimentary units. With the goal to investigate the impact of lithology on medium-enthalpy geothermal fluids, 15 hot spring discharges were sampled and analyzed for anthropogenic tracers and isotopic composition and compared to the analyses of 31 reservoir rock analogues. Comparison of strontium isotope signatures between rock analogues and hot spring discharges allow an allocation of associated reservoir rocks. Chlorofluorocarbons quantify the dilution of the geothermal springs by shallow groundwater, ranging from almost CFC-free samples to dilution with modern meteoric water by up to 50 %. Fluids discharging from plutonic rocks have low proportions of dilution with modern waters, while hot springs discharging from the volcano-sedimentary rocks have a higher and variable dilution with modern waters. The fractionation of oxygen isotopes of the SO_4-H_2O system reveals reservoir temperature estimates of 80–100 °C in the plutonic sequence matching discharge temperatures. For the springs discharging from volcano-sedimentary units higher reservoir temperatures of 100–140 °C are calculated. On basis of the analysis, a conceptual reservoir model can be derived. Fast fluid ascent is indicated along Liquiñe-Ofqui fault system in the NPB by similar discharge and reservoir temperatures and low surficial dilution rates. Large differences in discharge and reservoir temperatures in the Cura-Mallín formation along with a high influx of surficial water may be attributed to a more branched pathway pattern. In conclusion lithology maybe an important factor when coming to the utilisation of geothermal resources.

1. Introduction

Hydraulic, thermal and geochemical characteristics of a geothermal system are intrinsically related to the local permeability distribution. Natural permeability in geothermal systems is controlled by critically oriented faults or fractures in the ambient stress field directing fluid movement (e.g. Rowland and Sibson, 2004; Zoback, 2011). In a given regional stress pattern mechanical strength contrasts, caused by varying lithologies, may individually affect fracture mechanics resulting in different characteristics of fault or fracture zones (e.g. Meixner et al., 2014). A well-studied example in this context is the Armutlu peninsula in NW-Turkey (Eisenlohr, 1997), where the assembly of crystalline basement rocks, marble, and evaporites causes individual, lithological dependent circulation systems resulting in different hydrochemical compositions and reservoir temperatures. However, also in the case of a pure crystalline setting, such as the well investigated areas of the Black Forest region, SW-Germany, Stober and Bucher (1999) identified the coexistence of two flow systems with different hydraulic properties that can be related to lithological changes between granite and gneiss. Herein, the change in lithology is accompanied by a permeability contrast that limits the occurrence of thermal springs to granitic formations being generated by a deep circulation system extending down

DOI of original article: http://dx.doi.org/10.1016/j.geothermics.2018.03.006
* Corresponding author at: Institute of Applied Geosciences, Karlsruhe Institute of Technology (KIT), Adenauerring 20b, 76135 Karlsruhe, Germany.
E-mail address: sebastian.held@kit.edu (S. Held).

https://doi.org/10.1016/j.geothermics.2018.03.004
Received 17 October 2017; Received in revised form 1 March 2018; Accepted 9 March 2018
Available online 01 April 2018
0375-6505/

to a depth of 4 km. The gneiss complexes host low-temperature mineral springs only. The flow is concentrated on sparse, high-permeability conduits without great penetration depth. In both studies the lithological control on geothermal circulation was identified by strong variations in hydrochemical fluid composition.

In case of the geothermal system at the Villarrica volcano the lithology contrast between plutonic units of the North Patagonian Batholith and volcano-sedimentary rocks of the Cura-Mallín formation, cannot be recognized in the main fluid composition (Held et al., 2017). Investigating the interplay between tectonics and fluid composition in a regional study, the system was found to be partitioned, which was attributed exclusively to the location and orientation of major fault zones neglecting the lithological contrast (Sánchez et al. (2013). The formation of the hot spring fluids was investigated by interpretation of their composition (Held et al., 2017) identifying water-rock interaction as being the process governing the fluid composition of the hot springs. Magmatic processes affect the geothermal springs only to a minor extent revealed e.g. by results of the analysis of oxygen and hydrogen isotope signatures (Held et al., 2017; Sánchez et al., 2013). The absence of typical indications for a high-enthalpy geothermal reservoir (Held et al., 2015; Held et al., 2016) supports the image of a medium-enthalpy geothermal systems with limited magmatic input.

Within this study comprehensive, geochemical fluid and rock sampling and analysis were conducted on 31 potential reservoir rock analogues and 15 hot spring samples of the Villarrica geothermal system to trace the lithological transition in the fluids and determine its impact on the thermal fluids. Complementary to the previous studies the fluids are analyzed for Sr isotopes, chlorofluorocarbon (CFC) concentrations and $\delta^{18}O$ values of sulfate, while the rocks are analyzed for geochemical composition and Sr isotope signatures. The investigations are part of a large geoscientific research project including hydrochemical, geophysical and structural measurements. An estimation of reservoir temperatures including a site-specific re-evaluation of solute geothermometry is conducted in the second part of a joint hydrochemical investigation of the Villarrica geothermal system (Nitschke et al., 2018).

2. Geological setting

The lithological transition between the Cura-Mallín formation and the North Patagonian Batholith is located in the Southern Volcanic Zone (SVZ) of Southern Chile. Volcanism in SVZ is related to the subduction of the Nazca Plate beneath the South American Plate. Structural geology of the central and southern SVZ is dominated by the Liquiñe-Ofqui fault system (LOFS), a N-S to N10°E oriented fault system running along the volcanic arc (Cembrano et al., 1996). The stress pattern causes a dextral strike-slip movement on the LOFS. The fault system is accompanied by WNW-ESE oriented Andean Transverse Fault zones (ATF) (Pérez-Flores et al., 2016). These ATFs are disoriented with respect to the prevailing stress field and undergo sinistral strike-slip movement (Cembrano and Moreno, 1994). Between 37°–39°S, the Bíobío-Aluminé fault system (BAFS) and the Mocha-Villarrica fault zone (MVFZ) are prominent structures in WNW-ESE direction (Fig. 1a).

The research area around the WNW-ESE aligned Villarrica-Quetrupillán-Lanín volcanic chain (Fig. 1b) is characterized by a complex tectonic pattern of intersecting fault zones. The LOFS, oriented N-S to NNE-SSW in the Villarrica area, passes the volcanic chain between Villarrica and Quetrupillán volcanos (Fig. 1) (Moreno and Lara, 2008). The LOFS is offset by the MVFZ by a few kilometers (Lopez-Escobar et al., 1995), then splits into two legs and continues on both shores of the N-S oriented Lake Caburgua. A detailed depth study of the LOFS along the southern shore of Lake Caburgua using a magnetotelluric survey revealed a sub-vertical orientation in upper crustal levels (Held et al., 2016). A fault system width of < 3 km is modeled for the Caburgua segment in agreement with the determined values of 2 km near the Liquiñe village (Hervé, 1976). The > 300 km long MVFZ runs transverse to the Andean volcanic arc (e.g. Bohm et al., 2002). Detailed magnetotelluric investigations reveal a broad, northward dipping fault zone (Held et al., 2016). Pérez-Flores et al. (2016) expect reservoirs of magma or fluid associated with ATF as the misorientation regarding the regional stress field impede vertical permeability (Tardani et al., 2016).

South of the Villarrica-Quetrupillán-Lanín volcanic chain plutonic rocks of the North Patagonian Batholith (NPB) prevails (Hervé, 1984; Munizaga et al., 1988) (Fig. 1). The pluton was emplaced between 39°-47°S during episodic magmatic events between Late Jurassic and Pleistocene (Pankhurst et al., 1999). Two phases of intensive plutonism are dated to be of Cretaceous and Miocene age. The batholith complex consists of plutonic rocks of dioritic to tonalitic composition (Adriasola et al., 2005). North of the volcanic chain, the plutonic basement occurs subordinately only, being replaced by the volcano-sedimentary Cura-Mallín formation of Eocene to Miocene age (Jordan et al., 2001) (Fig. 1). The formation was deposited in a sequence of intra-arc basins in south central Chile (33°–39°S), which had developed under extensional tectonics between Eocene and Miocene (Charrier et al., 2007). The formation of up to 3000 m in thickness consists of two facies (Radic, 2010). The Rio Pedregoso facies is composed of lacustrine, deltaic and fluvial sediments, and is intercalated with the Guapitrío facies, a volcanic facies of pyroclastic deposits and lava flows (Suarez and Emparan, 1995). In the study area north of the volcanic chain, the Guapitrío facies dominates (Villalón, 2015). It is assumed that the Cura-Mallín formation hosts geothermal reservoirs in Southern Chile, e.g. the Tolhuaca geothermal system (Sánchez-Alfaro et al., 2016).

Subduction generates more than 60 Holocene stratovolcanoes in the SVZ, accompanied by a high number of minor eruptive complexes (Stern, 2004). Volcanic centers are spatially related to prominent structural weak zones (Lara et al., 2006). The active Villarrica volcano belongs to the WNW-ESE oriented volcanic chain, following the lineament of the MVFZ. Magma chambers are assumed to be located at upper and lower crustal depths below Villarrica Volcano (Hickey-Vargas et al., 1989). Unlike Quetrupillán and Lanín, Villarrica exhibits a strong, frequent activity of basaltic-andesitic composition with > 20 major eruptions per century (Petit-Breuilh and Lobato, 1994).

3. Materials and methods

In the surroundings of the Villarrica-Quetrupillán-Lanín volcanic chain, more than 20 hot springs discharge with temperatures of up to 80 °C (Hauser, 1997). Outflow conditions of the springs are described in detail by Pérez (1999). Often, at each location there are several springs with volume flow of around 1 L/s discharge varying slightly in terms of temperature and hydrochemical composition. The full hydrochemical dataset of the 15 sampled springs is presented in Held et al. (2017). Hence, we describe merely the complementary materials and methods required for the additional investigations. If not mentioned otherwise measurements are conducted at the Institute of Applied Geosciences at the Karlsruhe Institute of Technology (Germany). The thermal springs were sampled additionally to investigate chlorofluorocarbons and oxygen isotopes of sulfate species. Samples for CFC determination were collected in 1L glass bottles with metal lined caps. To protect the samples from atmospheric contamination, the bottles were enclosed by tight copper tins, also filled with sampling water. During sampling, copper tins and enclosed bottles were set on the base of a vessel (~10 L) and were filled with a tube from inside the glass bottle. A minimum of three bottle volumes were pumped through a tube from the bottom of the bottle before capping bottle and copper tin underwater. Three samples (Con, Tol and Bla, Fig. 1) were discarded, as in these cases contamination with atmospheric CFCs could not be excluded due to the outflow conditions (unknown equilibration state as discharging in hot pools). CFC analysis was performed at the Spurenstofflabor Dr. Harald Oster, Wachenheim, Germany, using purge and trap gas chromatography with an electron capture detector (GC-ECD).

In order to provide a sufficient amount of sulfate for the

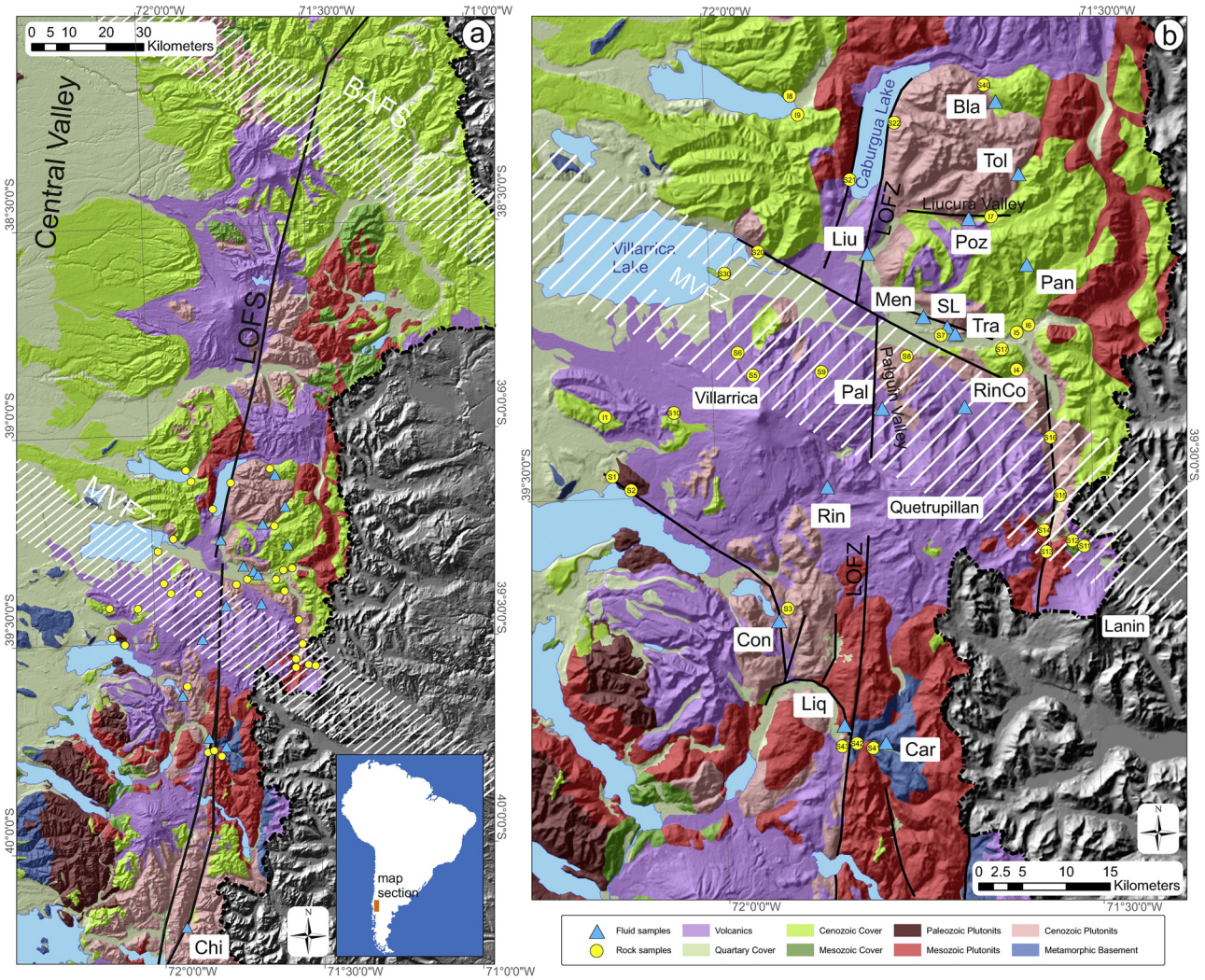

Fig. 1. a) Geological map of the volcanic arc of Southern Chile between 38.0°S − 40.4°S displaying outcrops of the NPB (reddish colors) in the south of the Villarrica-Quetrupillán-Lanín volcanic chain and volcano-sedimentary basin fillings (bright green color) of the Cura-Mallín formation north of it. Intra-arc LOFS (simplified in Figure a) crosscuts the NPB and continues to the N in the volcano-sedimentary sequence, intersected by Andean Transfer faults in the form of the BAFS and MVFZ. b) Research area showing rock (yellow circles) and fluid (blue triangles) sampling locations. Hot spring abbreviations are listed in Table 2. The location of Chi, which was additionally analyzed to increase sample number along LOFS, is depicted in Figure a. Faults in Figure b are taken from geological maps of the study area (Lara and Moreno, 2004; Moreno and Lara, 2008). A shaded relief map derived from CGIAR-CSI version of SRTM data. Geological map modified after 1:1′000′000 scale map, Servicio Nacional de Geología y Minería, Chile by including interpretations from Cembrano and Lara (2009), Sánchez et al. (2013), Moreno and Lara (2008), and Lara and Moreno (2004). (For interpretation of the references to colour in this figure legend, the reader is referred to the web version of this article.)

determination of $d^{18}O$ isotopes, 1L fluid samples were collected without further treatment stored in polyethylene vessels avoiding any head space. Total sulfate was precipitated as $BaSO_4$ by adding a stoichiometric excess of $BaCl_2$ before measuring oxygen isotope ratios of precipitates by isotope-ratio mass spectrometry (IRMS: GV Instruments IsoPrime combined with HTO Pyrolysis by HEKAtech measured at 1350 °C using the following standards NBS127, N3, V-SMOW, GISP, LK2, LK3).

31 rock samples were collected in the vicinity of the volcanic chain. Sampling locations were chosen to a) obtain a comprehensive collection of possible reservoir rock analogues of the research area and b) establish spatial relationships between thermal springs and nearby rocks. These circumstances result in the selection of outcrops (Fig. 1). Prior to analysis, the rock samples were ground-up using an agate disk mill. Main element concentrations were determined using wavelength-dispersive X-ray spectroscopy (Bruker AXS, S4 Explorer). Ground-up rock samples were analyzed for Rb and Sr concentrations by energy-dispersive X-ray fluorescence (Panalytical, Epsilon 5). Sr isotope ratios of rock samples were measured by the University of Tübingen, Isotope Geochemistry Group using thermal ionization mass spectrometry (TIMS: FinniganMAT 262).

4. Results and discussion

4.1. Analysis of reservoir rock analogues: potential host rocks of the geothermal system

The geochemistry of sampled rocks is analyzed to characterize the host rock interacting with the geothermal fluids. The analysis of reservoir rock analogues should identify geochemical variations between the different, igneous rock types that might be traced within the fluid signature. Element concentrations of the sampled reservoir rock analogues are summarized in Table 1. In the research area mainly three distinct rock types outcrop (Moreno and Lara, 2008): 1) plutonic rocks of dioritic to granitic composition belonging to NPB, 2) fresh volcanic rocks of rather uniform basaltic to andesitic composition 3) volcano-sedimentary units of the Cura-Mallín formation possessing highly variable SiO_2 concentrations, thus overlapping both, volcanic and

Table 1
Major element composition, concentrations of Rb and Sr, and $^{87}Sr/^{86}Sr$ isotope ratio of rock samples from Villarrica area. Classification according to rock type and age (VV, VL, VQ: Volcanic rock Villarrica/Lanín/Quetrupillán; PP: Paleozoic; plutonic rocks; MP: Mesozoic plutonic rock of NPB; CP: Cenozoic plutonic rock of NPB; MB: Metamorphic basement; MC: Mesozoic cover; CC: Cenozoic cover = Cura-Mallín formation). Age classification according to Moreno and Lara (2008 and Lara and Moreno (2004). n.m. = not measured

Sampling point	Latitude	Longitude	Rock class	Na_2O [%]	MgO [%]	Al_2O_3 [%]	SiO_2 [%]	P_2O_5 [%]	K_2O [%]	CaO [%]	TiO_2 [%]	MnO [%]	Fe_2O_3 [%]	LoI [%]	S	c(Rb) [ppm]	c(Sr) [ppm]	Rb/Sr	$^{87}Sr/^{86}Sr$	s $^{87}Sr/^{86}Sr$
S1	−72.13	−39.48	VV	2.31	4.54	17.56	48.95	0.02	0.47	8.90	1.15	0.17	11.39	2.11	97.59	n.m.	n.m.	n.m.	n.m.	n.m.
S2	−72.13	−39.49	PP	3.31	1.80	14.72	61.01	0.07	0.55	4.77	0.56	0.04	7.07	3.92	97.83	15.0	161.7	0.093	0.7072	± 0.000009
S3	−71.92	−39.63	CP	3.13	0.63	13.56	71.91	0.02	4.09	2.04	0.33	0.04	2.20	0.38	98.33	148.5	213.7	0.695	0.7044	± 0.000010
S5	−71.95	−39.38	VV	3.04	5.13	17.48	51.37	0.24	0.69	9.72	1.19	0.14	9.70	0.02	98.72	n.m.	n.m.	n.m.	n.m.	n.m.
S6	−71.97	−39.35	VV	2.86	6.40	16.65	51.19	0.20	0.64	9.63	1.12	0.15	9.94	0.12	98.90	15.8	416.4	0.038	0.7040	± 0.000008
S7	−71.69	−39.34	CP	4.15	0.49	14.24	71.63	0.05	3.04	2.07	0.26	0.05	2.19	0.71	98.89	75.6	209.7	0.361	0.7043	± 0.000010
S8	−71.74	−39.36	MP	3.71	1.26	13.37	71.40	0.08	1.98	1.50	0.35	0.06	3.10	1.68	98.50	75.0	291.2	0.258	0.7047	± 0.000010
S9	−71.86	−39.38	VV	3.48	3.38	17.30	55.23	0.18	0.82	7.86	1.03	0.15	9.05	0.14	98.61	18.9	421.7	0.045	0.7041	± 0.000010
S10	−72.05	−39.41	CC	3.30	2.88	17.04	57.20	0.17	0.85	6.48	0.71	0.15	6.79	2.81	98.40	36.3	549.0	0.066	0.7044	± 0.000008
S11	−71.51	−39.56	VL	3.13	5.15	17.47	49.97	0.34	1.21	8.45	1.25	0.17	10.85	0.34	98.33	33.7	664.9	0.051	0.7040	± 0.000010
S12	−71.53	−39.56	MC	3.56	0.71	13.60	70.11	0.05	3.32	1.94	0.25	0.05	2.68	2.08	98.35	124.8	152.2	0.820	0.7065	± 0.000010
S13	−71.56	−39.56	CP	3.56	3.70	17.65	54.49	0.24	1.03	7.36	0.96	0.13	7.39	1.46	97.98	27.6	500.7	0.055	0.7045	± 0.000009
S14	−71.57	−39.54	MP	3.17	3.57	16.63	56.24	0.17	2.24	6.34	0.77	0.12	6.96	2.00	98.20	88.5	374.0	0.237	0.7051	± 0.000010
S15	−71.54	−39.51	CP	3.60	3.57	16.92	56.91	0.21	1.35	6.43	0.95	0.20	6.23	2.07	98.44	n.m.	n.m.	n.m.	n.m.	n.m.
S16	−71.55	−39.45	VQ	4.54	2.55	16.84	56.56	0.44	1.67	5.90	1.21	0.17	7.92	0.66	98.46	35.6	550.4	0.065	0.7040	± 0.000090
S17	−71.62	−39.35	CC	3.50	0.43	13.17	73.17	0.01	3.78	1.35	0.24	0.05	1.76	1.05	98.50	118.6	190.8	0.621	0.7041	± 0.000011
S20	−71.93	−39.25	CP	2.73	2.02	13.71	65.77	0.06	1.77	5.03	0.52	0.09	5.40	1.16	98.25	54.8	201.9	0.271	0.7041	± 0.000009
S21	−71.81	−39.18	MP	2.20	0.09	11.69	73.97	0.01	4.11	2.58	0.13	0.04	1.50	1.77	98.10	138.0	265.2	0.520	0.7060	± 0.000010
S22	−71.75	−39.12	CP	3.81	2.62	17.01	57.91	0.27	1.63	6.13	0.88	0.11	6.46	0.93	97.75	55.7	576.2	0.097	0.7040	± 0.000008
S30	−71.98	−39.27	CC	1.66	4.29	19.37	44.58	0.03	0.16	10.00	0.48	0.13	7.39	9.20	97.28	16.5	384.5	0.043	0.7042	± 0.000009
S40	−71.63	−39.08	CP	3.96	0.20	12.29	76.48	0.00	3.76	0.38	0.15	0.02	0.74	0.65	98.64	n.m.	n.m.	n.m.	n.m.	n.m.
S41	−71.82	−39.76	MP	3.00	1.90	13.93	66.58	0.16	2.21	2.52	0.65	0.07	4.90	1.87	97.78	72.0	290.8	0.248	0.7130	± 0.000009
S42	−71.83	−39.76	MB	2.86	1.33	12.48	73.07	0.15	2.00	1.85	0.54	0.06	3.62	0.94	98.91	75.5	164.6	0.458	0.7174	± 0.000010
S43	−71.84	−39.76	CP	3.09	0.47	13.02	74.91	0.00	4.34	1.61	0.20	0.05	1.47	0.47	99.62	156.2	166.2	0.940	0.7085	± 0.000009
I1	−72.13	−39.40	CC	2.84	2.65	16.49	55.84	0.15	0.83	6.23	0.89	0.07	7.22	6.18	99.39	23.5	417.2	0.056	0.7041	± 0.000011
I4	−71.60	−39.39	CC	2.51	4.68	17.33	54.89	0.22	1.51	8.15	0.97	0.14	7.88	2.24	100.52	n.m.	n.m.	n.m.	n.m.	n.m.
I5	−71.58	−39.34	CC	2.99	4.28	17.84	52.17	0.34	1.18	8.26	1.24	0.17	9.49	2.30	100.26	35.8	597.5	0.060	0.7040	± 0.000009
I6	−71.60	−39.35	CC	3.70	0.95	14.23	72.35	0.09	4.13	1.96	0.41	0.07	2.52	1.03	101.43	136.6	221.1	0.618	0.7040	± 0.000009
I7	−71.64	−39.22	CC	3.23	1.56	14.34	65.98	0.15	1.92	4.12	0.61	0.10	4.34	4.90	101.25	71.4	175.8	0.406	0.7041	± 0.000010
I8	−71.90	−39.09	CC	3.87	5.02	19.02	49.74	0.27	0.78	6.38	1.32	0.11	9.49	3.98	99.97	14.7	547.6	0.027	0.7044	± 0.000007
I9	−71.88	−39.11	CC	4.65	0.93	14.23	62.68	0.23	0.73	3.59	0.57	0.21	7.13	2.10	97.05	18.3	352.0	0.052	0.7042	± 0.000009

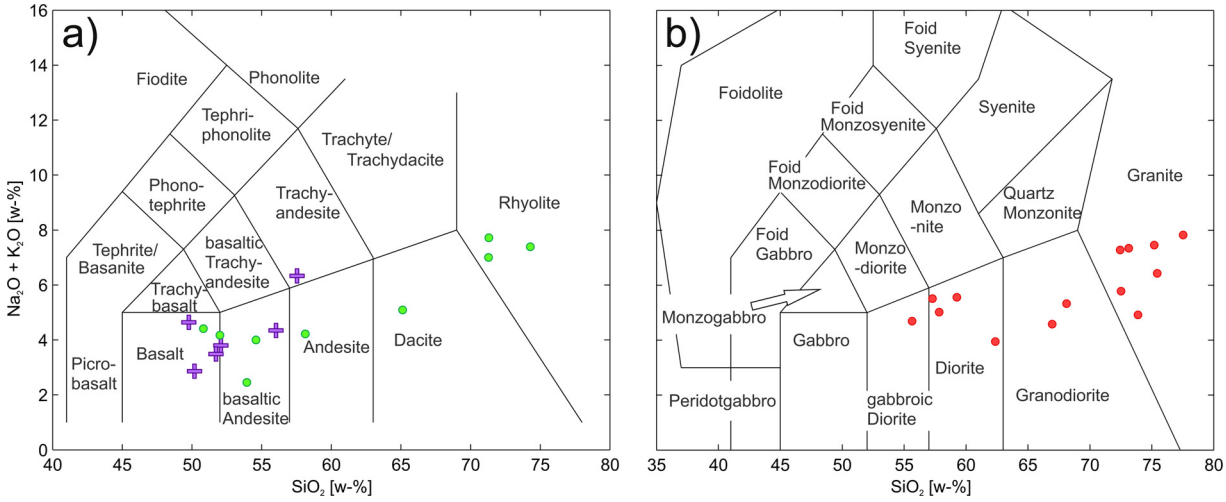

Fig. 2. Classification of sampled rocks using the TAS diagram for a) volcanic rocks (Le Maitre, 2005) and b) plutonic rocks (Middlemost, 1994). Volcanic rock samples are subdivided into volcanic rocks of recent activity (purple crosses) and volcano-sedimentary units (green circles). (For interpretation of the references to colour in this figure legend, the reader is referred to the web version of this article.)

plutonic rock facies (Fig. 2). In the study area the volcano-sedimentary unit is dominated by the volcanic Guapitrío facies, as the samples range from pure andesitic lava flows to volcanoclastic conglomerates and lahar deposits (Villalón, 2015).

The spatial distribution of collected rocks marks the gradual transition from pure occurrence of batholithic rocks south of the volcanic chain to volcano-sedimentary units of the Cura-Mallín formation alternating with plutonic outcrops north of the chain (Fig. 1). The occurrence of plutonic rocks does not cease north of the volcanic chain but is limited in size and incidence. North of the volcanic chain thermal springs often discharge at boundaries between plutonic and volcano-sedimentary rocks (Fig. 1). The fresh volcanic rocks cover plutonic or volcano-sedimentary rocks in the vicinity of volcanic edifices.

The elemental composition and its statistical variance of different rock classes is shown in Fig. 3 revealing the geochemical similarity between rocks of plutonic and volcano-sedimentary origin. Boxplots for SiO_2, Al_2O_3, Na_2O, MgO and CaO overlap extensively, significant differences occur only in terms of K_2O content. Yet it can be noted that recent volcanic rocks differ from plutonic or and volcano-sedimentary rocks, particularly MgO, CaO and Al_2O_3 concentrations. Despite this, allocation between geothermal fluid composition and related host rock geochemistry is masked, especially in this case of similar geochemical composition, by secondary processes (different solubilities of primary minerals, precipitation of alteration products, temperature-dependent cation exchange e.g. in feldspars) and thus deceptive.

As a consequence Rb and Sr are used for comparison between fluid and rock signature (see the following chapter). Rb and Sr can substitute for K and Ca in the rock matrix due to their similar atomic radius and charge (Faure, 1986). Rb and Sr concentrations of the reservoir rock analogues as well as $^{87}Sr/^{86}Sr$ ratios, which are be used in a combined approach, are listed in Table 1. Rb concentrations of the rock samples vary between 14.7 and 156 ppm with a positive correlation of Rb and K concentrations (Fig. 4b). Sr rock concentrations range between 152 and 664 ppm, with an apparent but less clear correlation of Sr and Ca (Fig. 4a). Plutonic rocks and K-rich volcano-sedimentary rocks (S12, S17, I6, I7) possess high Rb concentrations, while fresh volcanic rocks and the majority of the volcano-sedimentary rocks have low Rb concentrations. The opposite is observed for Sr and Ca concentrations: plutonic rocks and volcano-sedimentary rocks with low Ca-concentrations have comparably low Sr concentrations while volcanic and Ca-rich volcano-sedimentary rocks possess higher Sr concentrations.

4.2. Deduction of reservoir rock type using Rb/Sr and $^{87}Sr/^{86}Sr$ isotope ratios

Allocation between host rock and geothermal fluids can be derived from Sr isotope ratios in combination with Rb/Sr ratios (Cortecci et al., 2005; Graham, 1992), as the fluid adapts the Rb and Sr concentrations as well as $^{87}Sr/^{86}Sr$ ratios from the host rock. $^{87}Sr/^{86}Sr$, based on the radioactive β-decay of ^{87}Rb to ^{87}Sr, depends on decay time, hence rock ages, and initial Rb concentration. Rb concentration correlates often with K concentration as Rb substitutes K in a rock matrix due to similar atomic ratios and charge. $^{87}Sr/^{86}Sr$ isotope ratios are not affected by fractionation within the liquid phase (Stettler, 1977) thus preserving the rock signature. In geothermal fluids Rb behaves nearly conservatively (Graham, 1992), as shown by the near constant Rb/Cl ratios

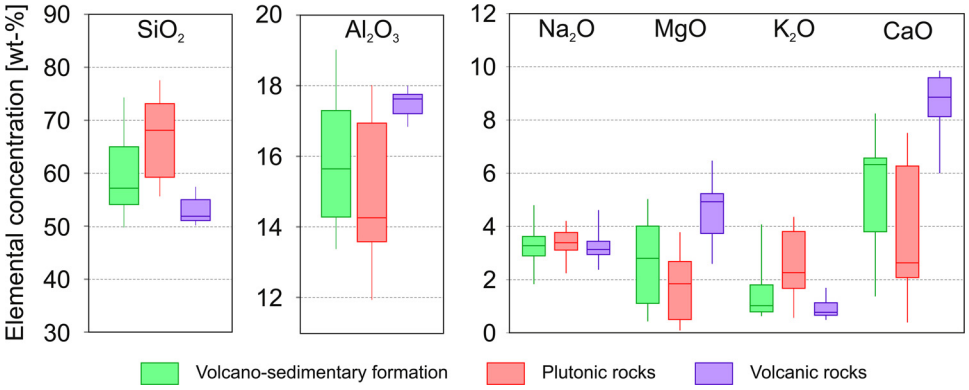

Fig. 3. Main elemental composition of reservoir rock analogues in boxplot display. Volcano-sedimentary and plutonic rocks have similar element distribution considering the variance in concentrations. (For interpretation of the references to colour in this figure legend, the reader is referred to the web version of this article.)

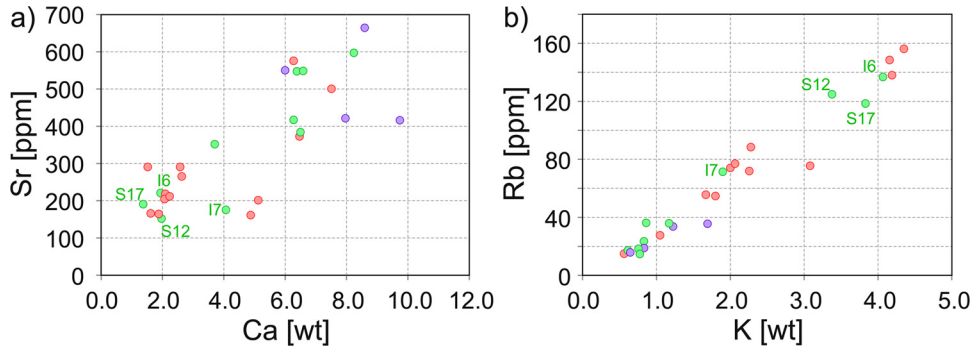

Fig. 4. a) Sr vs. Ca and b) Rb vs. K binary diagrams presenting the correlation between those elements in the rock samples (color code according to Fig. 3). (For interpretation of the references to colour in this figure legend, the reader is referred to the web version of this article.)

(Table 2), affected only within early stages of water-rock interaction by the uptake in illite before reaching full equilibrium (Giggenbach, 1991). Sr concentrations in geothermal fluids can, after equilibration and adaption of rock signature, be decreased by Sr incorporation in Ca-rich precipitates (e.g. calcite).

To differentiate between plutonic and basaltic host rocks, $^{87}Sr/^{86}Sr$ is often sufficient due to clearly separated isotope ratios. Presumably due to short decay times the Cenozoic rocks of NPB can possess low $^{87}Sr/^{86}Sr$ isotope ratios (generally not as low as volcanic rocks of basaltic origin but similar). The sampled Cenozoic plutonic rocks (S3, S7, S13, S20, S22) have low $^{87}Sr/^{86}Sr$ values between 0.7040-0.7045 (Table 1) overlapping in its minimum values volcanic signatures. To assure the distinction between plutonic and volcanic rocks Rb/Sr ratios are incorporated resulting in the Rb/Sr vs. $^{87}Sr/^{86}Sr$ diagram (Fig. 5).

Statistical evaluation of Rb/Sr and $^{87}Sr/^{86}Sr$ values for plutonic and volcanic rocks is conducted using relevant datasets for NPB (N = 212) (Mc-Millan et al., 1989; Munizaga et al., 1988; Pankhurst et al., 1992; Pankhurst et al., 1999) and volcanic rocks of major stratovolcanoes between 38.6°S and 40°S (N = 79) (Hickey-Vargas et al., 1989; Jacques et al., 2014; Mc-Millan et al., 1989). 2-D Boxplots are constructed reflecting areas of higher probability concerning Rb/Sr and $^{87}Sr/^{86}Sr$ ratios for each rock type. A significant differentiation between volcanic and plutonic rocks becomes obvious, as volcanic rocks have low Rb/Sr ratios (< 0.075) and narrow $^{87}Sr/^{86}Sr$ range while plutonic rocks generally have higher Rb/Sr ratios (> 0.21) and $^{87}Sr/^{86}Sr > 0.7045$ showing also a greater scattering. Nevertheless, overlaps of both probability fields exist documented by the whiskers. Literature data for the Cura-Mallín formation is not available.

The reservoir rock analogues of our survey at Villarrica-Quetrupillán-Lanín volcanic chain coincide with regional datasets (Fig. 5): volcanic rocks plot within a narrow volcanic box, while plutonic rocks have a higher scattering still coinciding with the plutonic probability field. The majority of the Cura-Mallín samples have low Rb/Sr ratios comparable to volcanic rocks with similar or slightly elevated $^{87}Sr/^{86}Sr$ ratios (0.7040-0.7045). Volcano-sedimentary rocks of elevated K and Rb concentrations (Fig. 4) have Rb/Sr ratios similar to plutonic rocks yet maintaining a low Sr isotope signature (I6, I7, S17 = 0.7040 − 0.7041).

Rb concentrations of spring discharges range from 5.5 to 51.9 mg/L, whereas Sr concentrations differ between 27.2 and 1100 mg/L. Sr isotope ratios of thermal spring waters exhibit variations between 0.7040 (SL) and 0.7112 (Car), whereas the local rain water has a ratio of 0.7063. The springs can be subdivided: 1) springs located within the plutonic field or exceeding it (Liq, Car) clearly related to water-rock interaction with plutonic rocks; 2) fluids of low Rb/Sr and $^{87}Sr/^{86}Sr$ ratios matching the signatures of volcanic or volcano-sedimentary rocks (Tol, Pan, Bla, Liu, Poz, Tra, SL); 3) hot spring fluids of elevated Rb/Sr ratios (0.2-0.6) but lowered $^{87}Sr/^{86}Sr$ ratios (Men, Rin, RinCo, Con, Pal). Whether the first two assignments are clear, the origin of the springs of lowered $^{87}Sr/^{86}Sr$ and elevated Rb/Sr ratios have to be discussed further. Possible origins are: a) interaction with plutonic rock of a low $^{87}Sr/^{86}Sr$ ratio; b) interaction with rocks of the Cura-Mallín formation possessing high Rb/Sr ratios; c) interaction with volcanic rocks in the state towards approaching full equilibrium and hence not depleted in terms of Rb; d) a mixture of fluids interacting with volcanic and plutonic rocks.

Although the origin of these springs could not be finally assigned, the lithology transition at the volcanic chain can be clearly traced. Springs south of the volcanic chain (Liq, Car) have Rb/Sr and $^{87}Sr/^{86}Sr$ signatures of fluids interacting with plutonic rocks, while the springs north of the chain (Tol, Pan, Liu, Poz, SL, Tra, Bla) have volcanic or volcano-sedimentary signatures. Considering the distribution of geological formations and the discharge location of the hot springs (Fig. 1), an interaction between those fluids and the volcano-sedimentary Cura-Mallín formation is indicated. The documented intermediate signatures of springs in the volcanic chain might indicate an interaction with both plutonic and volcanic or volcano-sedimentary rocks (option d) coinciding with the lithology transition.

4.3. Temperature dependent oxygen isotope fractionation of the SO_4-H_2O system

The oxygen isotope fractionation between H_2O and SO_4, due to its temperature dependence, is used as a tool to determine reservoir temperature (Hoering and Kennedy, 1957). The results of the method will be compared to the reservoir temperatures calculated after re-evaluation of geothermometric techniques carried out by Nitschke et al. (2018).

Fractionation of ^{18}O in the SO_4-water system as a geothermometric tool was chosen, as it is lithology independent in igneous systems. Hydrothermal alteration processes in such systems, usually in form of well-documented clay mineral precipitation or cation exchange reactions of the feldspars, do not affect the oxygen fractionation. SO_4 assimilation through leaching of evaporitic rocks or SO_4-rich groundwater would adversely affect temperature estimation (e.g. Cortecci, 1974), which can be neglected considering the absence of evaporitic rocks (Moreno and Lara, 2008). Modification of the oxygen isotope composition of SO_4 by dilution with shallow SO_4-rich groundwater is also negligible due to a low SO_4 concentration (< 5 % of thermal waters) of the local groundwater (Held et al., 2017). Reservoir processes affecting the oxygen isotope signatures, especially phase separation through boiling during decompression results in incorrect temperature estimations. Yet $\delta^{18}O(H_2O)$ evaluation (see $\delta^{18}O/\delta^{2}D$ diagram in Held et al. (2017)) indicates the absence of boiling in the Villarrica geothermal fluids, neglecting temperature estimation distortion. Impacts on oxygen isotope composition of H_2O by dilution with shallow groundwater cannot be excluded. Even with the quantification of dilution (see next chapter) its correction is not feasible due to the unknown oxygen isotope composition of the infiltrating fluid, which is difficult to determine in areas of pronounced relief. Equilibration

Table 2
Sampling locations, physico-chemical parameters, chemical composition, stable isotopes ($\delta^{18}O$ from H_2O and SO_4) and Sr isotope ratios from thermal springs around Villarrica volcano. Concentrations of solutes are given in mg/L, isotope ratios in ‰V-SMOW; n.m. = not measured, n.a. = not available, bdl. = below detection limit. Data for cation composition, Rb and Sr concentrations as well as $^{87}Sr/^{86}Sr$ and $\delta^{18}O$ (H_2O) are taken from Held et al. (2017) and listed for completeness. For the complete dataset see Held et al. (2017).

Sample		Carranco	Chihuio	Coñaripe	Liquine	Liucura	Los Pozones	Menetue	Palguin
Label		Car	Chi	Con	Liq	Liu	Poz	Men	Pal
Latitude	[°S]	−39.7654	−40.1939	−39.6349	−39.7394	−39.2595	−39.2263	−39.3291	−39.4197
Longitude	[°W]	−71.7922	−71.9345	−71.9239	−71.8429	−71.7926	−71.6513	−71.7193	−71.7830
Altitude	[masl]	450	312	260	328	618	736	336	477
T	[°C]	82.0	85.0	71.7	71.0	29.5	53.1	50.5	47.5
pH		8.9	8.9	7.8	9.1	7.9	9.1	9.3	8.7
TDS	[mg/L]	375	485	524	338	304	295	312	292
Cl	[mg/L]	34.1	13.9	82.9	17.4	35.3	46.2	26.2	21.1
Rb	[mg/L]	23.5	15.8	23.9	23.8	6.81	12.9	14.0	9.39
Sr	[mg/L]	74.0	331	60.4	65.9	83.9	168	58.6	27.2
Rb/Sr		0.318	0.048	0.396	0.361	0.081	0.077	0.239	0.345
$^{87}Sr/^{86}Sr$		0.71124	0.70425	0.70410	0.70620	0.70419	0.70413	0.70411	0.70452
σ $^{87}Sr/^{86}Sr$		± 9.0E-6	± 9.0E-6	± 1.2E-5	± 1.3E-5	± 8.0E-6	± 8.0E-6	± 1.3E-5	± 1.3E-5
$\delta^{18}O$ (H_2O)	[‰V-SMOW]	−9.92	−10.25	−8.10	−9.45	−9.07	−10.24	−9.04	−9.87
σ $\delta^{18}O$ (H_2O)	[‰V-SMOW]	± 0.06	± 0.03	± 0.02	± 0.04	± 0.03	± 0.03	± 0.00	± 0.06
$\delta^{18}O$ (SO_4)	[‰V-SMOW]	3.19	2.11	0.63	3.78	2.55	−0.68	1.55	0.74
σ $\delta^{18}O$ (SO_4)	[‰V-SMOW]	± 0.05	± 0.1	± 0.14	± 0.1	± 0.23	± 0.19	± 0.04	± 0.16
CFC-11	[pmol/L]	0.43	0.22	n.m.	0.32	2.2	0.6	0.5	0.8
σ CFC-11	[pmol/L]	± 0.05	± 0.05	n.m.	± 0.05	± 0.3	± 0.1	± 0.1	± 0.1
CFC-12	[pmol/L]	0.34	0.14	n.m.	0.2	1.3	0.37	0.36	0.52
σ CFC-12	[pmol/L]	± 0.05	± 0.05	n.m.	± 0.05	± 0.1	± 0.05	± 0.05	± 0.05
CFC-113	[pmol/L]	0.05	0.03	n.m.	0.04	0.2	0.06	0.05	0.07
σ CFC-113	[pmol/L]	± 0.05	± 0.05	n.m.	± 0.05	± 0.05	± 0.05	± 0.05	± 0.05

Sample	Panqui	Rincon	Rinconada	Rio Blanco	San Luis	Toledo	Trancura	Lake Villarrica	Rainwater Caburgua
Label	Pan	Rin	RinCo	Bla	SL	Tol	Tra	Lake	Rain
Latitude	−39.2534	−39.5077	−39.4215	−39.108-6	−39.3400	−39.1802	−39.340-2	−39.2723	−39.2199
Longitude	−71.5306	−71.8543	−71.6696	−71.613-6	−71.6906	−71.5849	−71.694-6	−71.9800	−71.8153
Altitude	926	939	605	733	429	920	372	240	420
T	50.8	37.5	27.6	54.1	41.0	42.5	36.0	15.5	n.m.
pH	8.0	7.6	6.1	7.7	9.1	7.8	9.0	7.9	7.6
TDS	390	375	788	400	236	871	229	75	37
Cl	25.5	20.9	40.6	21.8	7.86	109	8.08	2.26	1.48
Rb	13.6	21.1	28.3	9.26	6.67	51.9	5.49	2.70	0.352
Sr	313	35.9	105	339	72.6	1100	70.0	24.6	4.47
Rb/Sr	0.043	0.588	0.270	0.027	0.092	0.047	0.078	0.110	0.079
$^{87}Sr/^{86}Sr$	0.70408	0.70413	0.70406	0.70442	0.70400	0.70407	0.70413	0.70417	0.70632
σ $^{87}Sr/^{86}Sr$	± 1.0E-5	± 1.3E-5	± 8.0E-6	± 1.0E-5	± 1.2E-5	± 1.0E-5	± 1.2E-5	± 1.3E-5	± 9.0E-6
$\delta^{18}O$ (H_2O)	−10.38	−9.74	−11.08	−10.13	−9.25	−10.41	−9.21	−8.57	−7.79
σ $\delta^{18}O$ (H_2O)	± 0.00	± 0.04	± 0.14	± 0.05	± 0.04	± 0.02	± 0.04	± 0.05	± 0.06
$\delta^{18}O$ (SO_4)	−1.99	0.33	0.56	0.85	0.04	−1.95	0.14	n.a.	n.a.
σ $\delta^{18}O$ (SO_4)	± 0.34	± 0.19	± 0.15	± 0.28	± 0.21	± 0.09	± 0.17	n.a.	n.a.
CFC-11	0.7	1.6	1.7	n.m.	1.2	n.m.	1.1	3.5	n.m.
σ CFC-11	± 0.1	± 0.2	± 0.2	n.m.	± 0.2	n.m.	± 0.2	± 0.4	n.m.
CFC-12	0.49	0.88	1	n.m.	0.72	n.m.	0.73	2.1	n.m.
σ CFC-12	± 0.05	± 0.05	± 0.1	n.m.	± 0.05	n.m.	± 0.05	± 0.2	n.m.
CFC-113	0.06	0.13	0.15	n.m.	0.1	n.m.	0.09	0.32	n.m.
σ CFC-113	± 0.05	± 0.05	± 0.05	n.m.	± 0.05	n.m.	± 0.05	± 0.05	n.m.

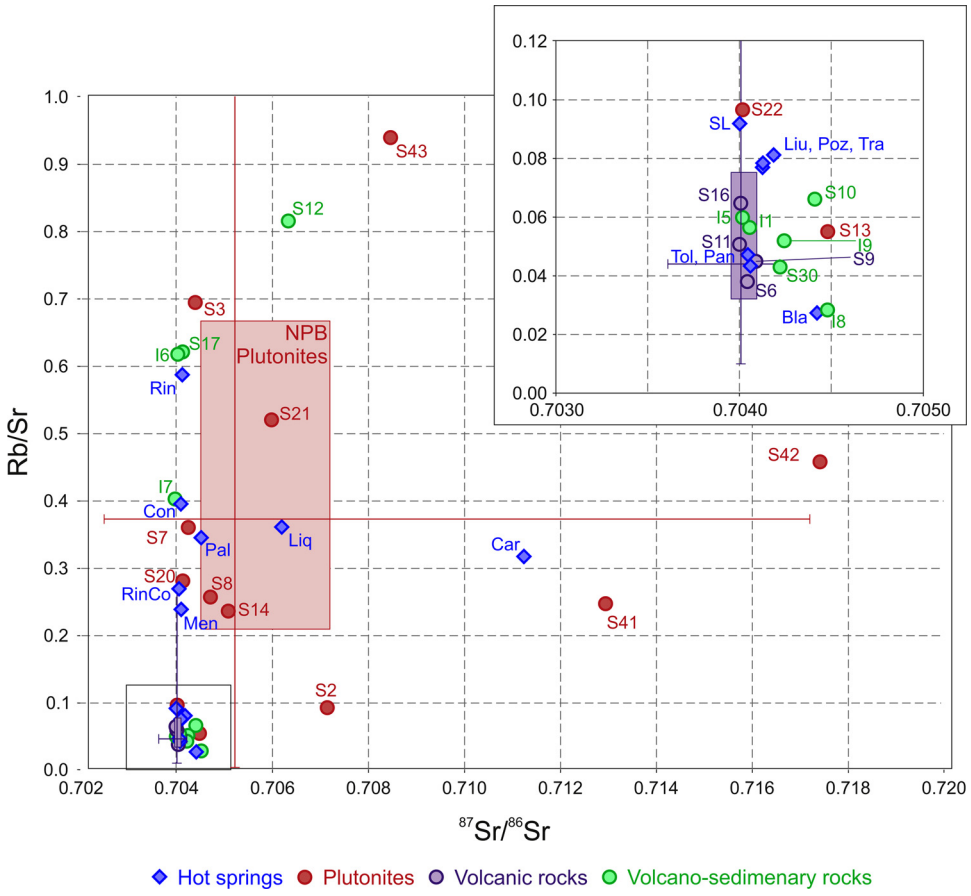

Fig. 5. Rb/Sr vs. $^{87}Sr/^{86}Sr$ plot for hot spring discharges (blue diamonds) and rock samples (circles, colorcode according to Fig. 3) from the Villarrica area. Additionally statistical relevant datasets for Rb/Sr and $^{87}Sr/^{86}Sr$ ratios are incorporated for NPB (N = 212) (Mc-Millan et al., 1989; Munizaga et al., 1988; Pankhurst et al., 1992; Pankhurst et al., 1999) and volcanic rocks of major stratovolcanoes between −38.6°S and −40°S (N = 79) (Hickey-Vargas et al., 1989; Jacques et al., 2014; Mc-Millan et al., 1989). The data is presented in 2-D boxplots for NPB (red) and volcanic rocks (purple). Chihuío hot spring not included as no outcrops of nearby rocks were collected. Signature of S12 has to be considered carefully as Mesozoic sedimentary rocks occur only sparsely in a restricted area near the Lanín volcano without clear relation to geothermal fluids. (For interpretation of the references to colour in this figure legend, the reader is referred to the web version of this article.)

kinetics of oxygen fractionation is rather fast under conditions of a medium- and high-temperature geothermal reservoir (Hoering and Kennedy, 1957) decreasing strongly at low ambient temperatures (Lloyd, 1968; Zhonghe, 2001). For geothermal applications the kinetics implicate that temperature estimation of low-enthalpy reservoirs will fail but for medium- and high-temperature reservoirs the temperature estimation will not be masked by re-equilibration in shallow reservoirs, being known e.g. from the K/Mg geothermometer (Giggenbach, 1991).

Oxygen isotope ratios of fluids range between −8.1 and −11.1 ‰V-SMOW and for SO_4 vary between 3.78 and 1.99 ‰V-SMOW (Table 2). The fractionation factor α can be calculated as:

$$\alpha = \frac{10^3\delta^{18}O(SO_4^{2-})}{10^3\delta^{18}O(H_2O)} \quad (1)$$

Geothermometer equations and, hence, equilibrium conditions have to be selected according to the sulfate species (SO_4^{2-}, HSO_4^-, H_2SO_4) and physicochemical parameters prevailing in the reservoir (Boschetti, 2013). For the expected medium-enthalpy system < 200 °C (Held et al., 2015; Sánchez et al., 2013) and pH > 5, SO_4^{2-} is the dominant species, resulting in the selection of equations according to Zeebe (2010) and Halas and Pluta (2000).

Oxygen fractionation of the SO_4^{2-}-H_2O system is evaluated using the method firstly described by Boschetti (2013) and applied by e.g. in Awaleh et al. (2015, 2017), with the fractionation coefficient being plotted versus discharge temperature (Fig. 6). The distribution of our data suggests two clusters. Samples Liq, Car and Chi plot close to the equilibrium line, indicating similarity between reservoir and discharge temperatures. Temperature estimations from oxygen isotope fractionation are in accordance with re-evaluated temperature estimations from SiO_2 and Na/K geothermometers in the range of 83–94 °C (Table 3) (Nitschke et al., 2018). These springs are located south of the volcanic chain along the LOFS in the plutonic sequence. It seems that

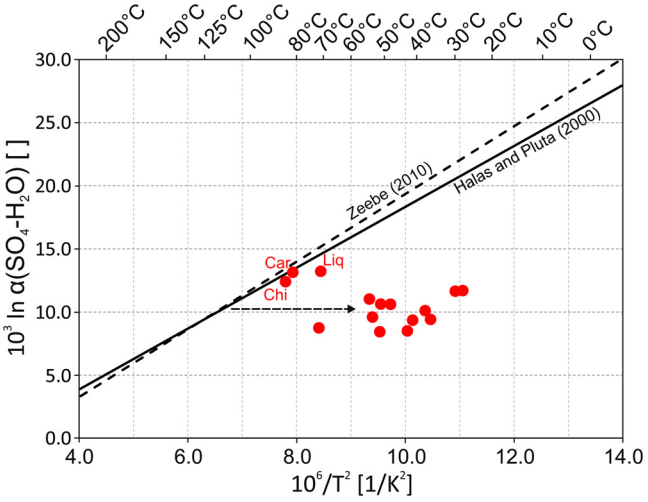

Fig. 6. Evaluation of oxygen isotope fractionation by depicting the fractionation factor α over discharge temperature. Reservoir temperature can be estimated by horizontal projection to geothermometer equations after Halas and Pluta (2000) or Zeebe (2010). As a consequence, the depicted dashed, horizontal arrow represents conductive cooling. (For interpretation of the references to colour in this figure legend, the reader is referred to the web version of this article.)

the fluids are not affected by cooling during ascent.

The majority of springs display a shift from equilibrium pointing to a significantly higher equilibration temperature compared to the discharge temperature. These springs are located in the volcanic chain or north of it. The reservoir temperatures, calculated by oxygen isotope fractionation are significantly higher (100–140 °C) than for springs in

Table 3
Reservoir temperature estimations calculated using the geothermometer based on oxygen isotope fractionation of the SO_4-water system. Calculations of fractionation factor α and temperatures after the formulas of Zeebe (2010) and Halas and Pluta (2000). Comparison to cation geothermometers is carried out in detail in Nitschke et al. (2018).

Sample	a	Zeebe (2010) T [°C]	Halas and Pluta (2000) T [°C]
Carranco	1.0132	88	84
Chihuio	1.0125	94	91
Conaripe	1.0088	134	134
Liquine	1.0133	87	83
Liucura	1.0117	101	99
Loz Pozones	1.0097	123	123
Menetue	1.0107	112	110
Palguin	1.0107	112	110
Panqui	1.0085	138	139
Rincon	1.0102	117	116
Rinconanda	1.0118	101	98
Rio Blanco	1.0111	108	106
San Luis	1.0094	126	126
Toldeo	1.0085	137	138
Trancura	1.0095	125	125

the plutonic sequence. Conformity between temperature estimates from oxygen isotope fractionation and re-evaluated solute geothermometer is obtained, the few outliers are discussed in Nitschke et al. (2018).

4.4. Estimating surficial dilution using chlorofluorocarbons (CFCs)

Anthropogenic tracers with evolving atmospheric concentrations can be used to estimate subsurface residence times and the mixing of different fluid bodies. Usually tritium is the method of choice, but as tritium input into the southern hemisphere is low due to the limited number of nuclear tests there and, hence, produces ambiguous results, we selected chlorofluorocarbons as anthropogenic tracers. Emission of CFCs began in the 1940s with the usage as refrigerants or propellants resulting in an increase of atmospheric and subsequently groundwater concentration. After the Montreal protocol, CFCs were replaced resulting in a decrease of atmospheric concentrations (Fig. 7).

CFC concentrations in the geothermal spring discharges are reported in Table 2. All samples of thermal springs and meteoric waters contain CFCs. As expected, high concentrations are observed in meteoric samples (Lake Pucón: e.g. CFC11 = 3.5 pmol/L) due to a continuous exchange with the atmosphere. Geothermal springs have lower values (e.g. CFC11 = 0.22 − 2.2 pmol/L). Particularly low values of CFC11 < 0.5 pmol/L are observed for springs south of the volcanic chain (Liq, Car, Chi). For comparison to atmospheric concentrations aqueous concentrations [pmol/L] of fluids determined are converted into atmospheric concentrations [pptv] using Eq. (2) (Plummer and Busenberg, 2006).

$$C_i = K_{H,i}{}^{*}\chi_i(P - p_{H_2O}) \quad (2)$$

where C_i is the aqueous concentration of each CFC, $K_{H,i}$ is the CFC specific Henry's law constant dependent upon TDS and temperature, c_i the dry air mole fraction of each CFC, P the elevation-depended total atmospheric pressure and p_{H2O} the temperature-dependent water vapor pressure. Results of the conversion are shown in Table 4. The results of selected springs are presented in comparison to atmospheric concentration evolution in the southern hemisphere in Fig. 7. Direct age determination (simple matching of fluid and atmospheric concentrations as presented by Plummer and Busenberg (2006)) yields non-modern infiltration. Consistently CFC-11 and CFC-12 values for thermal springs yield similar age estimations (e.g. Pan: age(CFC-11) = 1967.5; age(CFC-12) = 1969), with younger infiltration ages being obtained from CFC-113 (Pan: age(CFC-11) = 1975). This discrepancy is, according to Plummer and Busenberg (2006), an indication of subsurface mixing processes. Thus, in the following section subsurface flow is investigated with respect to mixing processes comparing observed CFC concentrations of hot springs with theoretical groundwater concentrations of different subsurface mixing models.

Anthropogenic tracers determined in thermal springs reflect a flux-averaged mixture of differently aged fluids (Gardner et al., 2011). The mixing of groundwater depends on the mixing processes (Turnadge and Smerdon, 2014). We compare no-mixing, piston flow to binary mixing and exponential mixing.

Binary mixing (Eq. (3)) is an end-member mixture of two differentially weighted (χ) water bodies of different infiltrations ages and, hence, different input concentrations (C_1, C_2) resulting in the observed concentration C_{obs}.

$$C_{obs} = C_1\chi + C_2(1 - \chi) \quad (3)$$

In the geothermal context, binary mixing reflects the mixing of old and hence CFC-free reservoir fluid with CFC bearing meteoric groundwater. This approach represents the mixing of the thermal fluid crossing shallow groundwater during ascent. Exponential mixing (Eq. (4)) describes complete mixing of multiple water bodies with different infiltration ages and hence CFC content. In the geothermal context, it displays a flow system of variable flow paths and/or the progressive addition of meteoric water to the geothermal reservoir. The observed CFC concentration $C(t_{obs})$ represents the average concentrations with a mean subsurface transient time τ (Małoszewski and Zuber, 1982).

$$C(t_{obs}) = \int_0^{\infty} C_{atmos}(t_{obs} - t')e^{-\lambda t'}\frac{1}{\tau}e^{\frac{t'}{\tau}}dt' \quad (4)$$

where C_{atmos} is the date-specific infiltrated CFC concentration, t_{obs} the time of observation, t' is the integration variable representing the infiltration age of each water portion and the exponential term accounts for first-order decay with half-life λ (included when appropriate e.g. in terms of intense bacterial reduction).

In the first step, it is tested whether subsurface mixing can be described by the binary mixing approach (Fig. 8), while in a second step exponential mixing is evaluated (Fig. 9). In Fig. 8 analyzed CFC concentrations of hot spring waters are compared with theoretical fluid concentrations of (1) no-mixing fluid flow (piston-Flow) or (2) binary mixing. The binary mixing line (Eq. (2)) is constructed by the connection of CFC-free fluid (c(CFC) = 0) with the CFC signature of recently

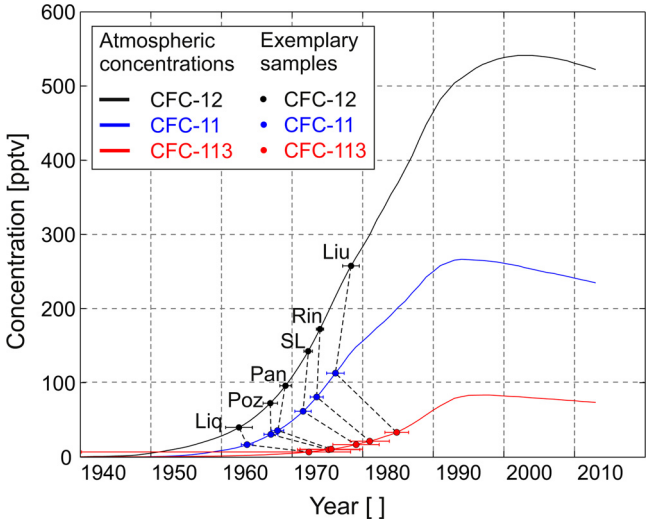

Fig. 7. Evolution of atmospheric concentrations of CFCs (CFC-11, CFC12, CFC-113) in the southern hemisphere. Data averaged from Plummer and Busenberg (2006) and NOAA (2015). Results for selected springs (Liq, Liu, Pan, Poz, Rin, SL) are converted into atmospheric concentrations [pptv] (see text). (For interpretation of the references to colour in this figure legend, the reader is referred to the web version of this article.)

Table 4
Results of subsurface mixing analysis. Binary mixing determines proportions of old, CFC-free fluid, while exponential mixing displays the mixing by mean transit time averaging residence times of different fluid bodies. Not shown are analyses of Coñaripe, Rio Blanco and Toledo hot springs as contamination with atmospheric CFCs could not be excluded.

Hot spring	Label	CFC-11 [pptv]		CFC-12 [pptv]		CFC-113 [pptv]		Binary mixing [% old CFC-free]	Exponential mixing Mean transit time [a]
Carranco	Car	21.7	± 2.5	66.5	± 9.8	8.1	± 8.1	90 ± 0.5%	300–400
Chihuio	Chi	11.1	± 2.5	27.4	± 9.8	4.9	± 8.1	96 ± 0.5%	> 500
Lake Pucon	Lake	179.4	± 20.5	415.9	± 39.6	52.9	± 8.3		
Liquine	Liq	16.4	± 2.6	39.6	± 9.9	6.6	± 8.3	93 ± 0.5%	450–550
Liucura	Liu	112.7	± 15.4	257.4	± 19.8	33.1	± 8.3	51 ± 4%	50–60
Los Pozones	Poz	30.2	± 5.0	72.3	± 9.8	9.7	± 8.1	86.5 ± 1.5%	200–300
Menetue	Men	25.6	± 5.1	71.3	± 9.9	8.3	± 8.3	88 ± 1.5%	300–400
Palguin	Pal	40.3	± 5.0	101.6	± 9.8	11.3	± 8.1	82 ± 2%	170–190
Panqui	Pan	35.3	± 5.0	95.9	± 9.8	9.7	± 8.1	83 ± 0.5%	180–210
Rincon	Rin	80.6	± 10.1	172.1	± 9.8	21.0	± 8.1	67 ± 2%	80–100
Rinconada	RinCo	84.4	± 9.9	193.8	± 19.4	23.8	± 7.9	63 ± 4%	80–90
San Luis	SL	61.5	± 10.2	142.5	± 9.9	16.5	± 8.3	73 ± 2.5%	110–120
Trancura	Tra	56.2	± 10.2	144.2	± 9.9	14.8	± 8.2	72.5 ± 3%	120–140

infiltrated groundwater (assumed infiltration age = 2013) (Fig. 8). For the CFC-11/CFC-12 system (Fig. 8a) CFC concentrations of thermal discharges match the Piston-Flow and partially also the binary mixing approach. However, when considering the remaining concentration plots, a discrepancy becomes obvious (Fig. 8b and c). Here the binary mixing and the measured CFC concentrations show a significant coincidence, whereas the Piston-Flow fluid movement is not the process generating hot spring waters of the Villarrica system. All thermal springs (also those not presented) match the constructed binary mixing curve within the range of the errors. Mixing ratios of old, CFC-free and meteoric fluids in exchange with recent atmospheric CFC concentrations can be derived from the positions along the binary mixing curve. Proportions from 50 to 96% of old fluid are determined for the analyzed samples (Table 4). Higher degrees (> 90%) of an old, CFC-free fraction are determined for springs along the LOFS in the plutonic sequence (Chi, Liq, Car).

Exponential mixing curves, additionally displaying exemplary mean transient times, are plotted in Fig. 9. Fluids, resulting from a mixing process based on an exponential mixing model, can be characterized by the mean transient time τ, averaging the ages of mixed water bodies. The CFC concentrations of thermal spring waters match the exponential mixing curve within the range of errors. Mean transient times of 50–500 a are determined (Table 4). As expected and in coincidence with results from binary mixing high mean transit times are calculated for springs along the LOFS (Liq, Car, Chi).

4.5. Comprehensive discussion and conceptual model

The results of analysis of CFC concentrations reveals that subsurface mixing strongly affects the circulation system. It becomes obvious that the mixing process (binary end-member mixing or continuous exponential mixing) cannot be resolved as the two theoretical mixing lines have only minor deviations and, hence, CFC signatures of the hot springs match both mixing lines.

Considering the measured local heat flow density of q_0 = 132–168 mW m^{-2} (Hamza and Muñoz, 1996) and assuming a thermal conductivity range of λ = 2.0–3.0 W m^{-1} K^{-1} (e.g. Eppelbaum et al., 2014) and a radioactive heat production range of A = 0.5–3 mW m^{-3} (e.g. Jaupart et al., 2016; Rybach, 1976) for crustal rocks, the reservoir depth can be constrainted to z = 1600–3100 m considering the estimated maximum reservoir temperatures of 140 °C. For geothermal fluids of comparable reservoirs, infiltration ages typically > 1000 a are determined, often even exceeding 10000 a (e.g. Morikawa, 2005; Pearson, 1991; Waber et al., 2017; Yokochi et al., 2013). Mean transient time of 50–500 a, as required to fulfil the CFC signatures of the fluids in terms of exponential mixing, conflicts with observations for geothermal circulation systems worldwide. As a consequence we believe that binary mixing between a deep CFC-free geothermal fluid and shallow groundwater with a modern CFC signature is most likely to reflect the subsurface mixing process. This mixing takes place during ascent of the geothermal fluid to the surface.

The lithology transition affects the geothermal circulation systems. In the plutonic sequence south of the volcanic chain, hot springs (Chi,

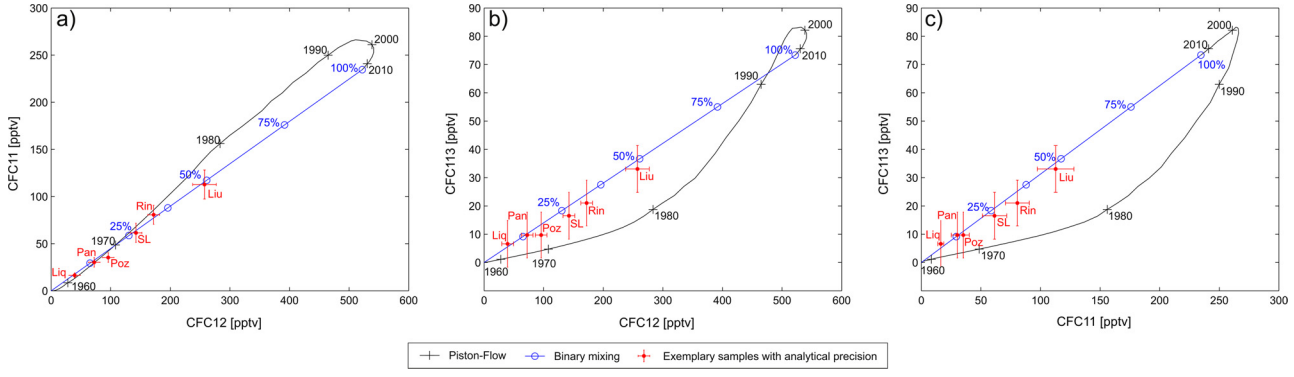

Fig. 8. Tracer plots comparing a) CFC-11 vs. CFC-12, b) CFC-12 vs. CFC-113, and c) CFC-11 vs. CFC-113 for southern hemisphere atmospheric input concentrations. Black lines represent the Piston-Flow approach with selected infiltration ages (+). The blue lines depict binary mixing of modern water, infiltrated 2013 with pre-modern, CFC-free water. Blue circles representing different mixing ratios. Red dots show analyzed CFC concentrations of selected thermal fluids. For legibility, only selected springs are displayed, full results in Table 4. (For interpretation of the references to colour in this figure legend, the reader is referred to the web version of this article.)

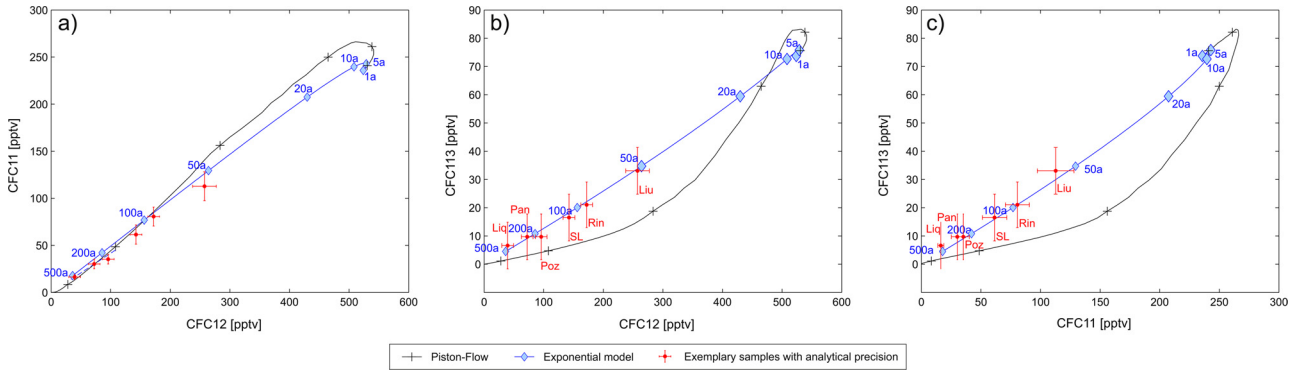

Fig. 9. Tracer plots comparing a) CFC-11 vs. CFC-12, b) CFC-12 vs. CFC-113, and c) CFC-11 vs. CFC-113 for southern hemisphere atmospheric input concentrations. Black lines represent the Piston-Flow approach with selected infiltration ages (+) for orientation. Blue lines depict exponential mixing with varying mean transient times (diamonds). Red dots show CFC concentrations of selected thermal fluids. Full results can be taken from Table 4. (For interpretation of the references to colour in this figure legend, the reader is referred to the web version of this article.)

Liq, Car) occur along the distinct run of the LOFS master fault. The highest percentages of the old fluid fraction are observed from results of CFC analysis. In combination with the (quasi) equality between reservoir and discharge temperature we conclude a highly channeled fluid ascent, presumably taking place on distinct, permeable fault zones. At the volcanic chain and to the north of it, the hot springs, discharging from volcanic or volcano-sedimentary formations, have higher and more variable proportions of mixing with meteoric waters. The hot springs have a more disperse spatial distribution often associated with secondary faults, fractures or lithology boundaries. In combination with the discrepancy between reservoir and discharge temperatures a branched, less focused fluid circuit is indicated. The differences in fluid pathways may be related to the different responses of the lithologies to the regional stress field. For instance, a similar behavior is inferred for the differences between gneisses and granites in the Black Forest by Stober and Bucher (1999), where the development of deep conduits is limited to granitic bodies.

Reservoir temperature estimations from oxygen fractionation of the H_2O-SO_4 system are in good agreement with refined solute (Nitschke et al., 2018) and multi-component geothermometric methods (Nitschke et al., 2017). In these studies, on selected springs in the volcanic chain (RinCo, Rin) higher temperatures (up to 180 °C) are estimated in agreement with maximum temperature estimations for the Geometricas hot spring (Sánchez et al. (2013). From all methods used, the following reservoir temperatures can be derived: a) 80–100 °C for springs along the LOFS in plutonic rocks, b) 100–140 °C for springs north of the volcanic chain and c) elevated temperatures (up to 180 °C) for some springs in the volcanic chain. The low discharge temperatures in group b) cannot be explained by higher dilution rates with shallow, cold groundwater alone, since linear temperature extrapolation towards 100% CFC-free fluid does not yield the determined reservoir temperatures (Fig. 10). Hence, a combination of conductive cooling and cooling by mixing with meteoric groundwater causes the decrease in the outflow temperature.

The origin of the different reservoir temperatures in plutonic and volcano-sedimentary formations might be related to: A) different basal heat flow q_0; B) variations in circulation depth of the geothermal fluids or C) different heat conductivities λ of the two lithologies. Whether the two first options are possible, option C is doubtful, as higher reservoir temperatures in the volcano-sedimentary formations would require higher heat conductivities of these rocks keeping the remaining parameters (A, q_0, z) constant. Yet in general plutonic rocks have heat conductivities exceeding that of volcanic rocks (e.g. Eppelbaum et al., 2014). The elevated temperatures in the volcanic chain might result from a limited, local intrusion of volcanic volatiles generated by magmatic degassing (Held et al., 2017) or a locally enhanced geothermal gradient both possibly related to the volcanic activity of the Villarrica volcano.

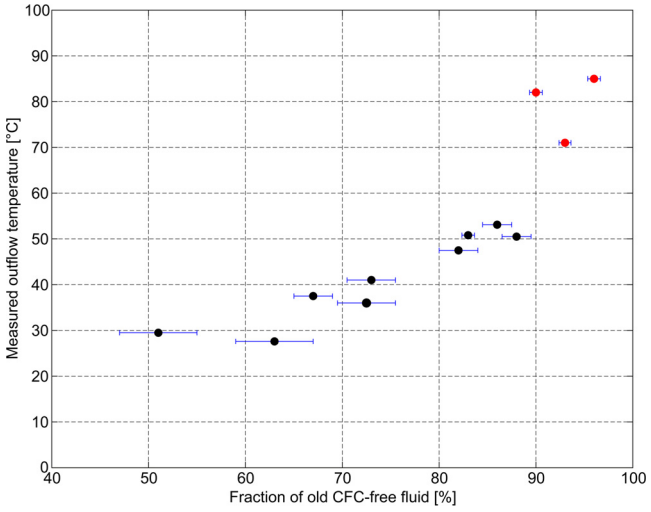

Fig. 10. Evaluation of subsurface cooling presented by plotting the ratio of old fluid, determined from CFC investigations vs. discharge temperature. Red circles: Springs south of the volcanic chain along the LOFS; black circles: Springs north of or along the volcanic chain; blue: Error bars of fraction estimation. (For interpretation of the references to colour in this figure legend, the reader is referred to the web version of this article.)

In the following a conceptual model summarizing all studies of the Villarrica geothermal system (Held et al., 2015; Held et al., 2016; Held et al., 2017; Nitschke et al., 2017, 2018; Sánchez et al., 2013) is presented (Fig. 11). The geothermal system is located at the intersection of LOFS with WNW-ESE oriented Andean Transfer faults (MVFZ and secondary faults). For the Caburgua segment a sub-vertical LOFS, < 3 km in width, is revealed by magnetotellurics presumably forming a flower structure. For the MVFZ a north dipping structure below the volcanic chain is detected by MT measurements. The medium enthalpy geothermal system is recharged by meteoric water. Fluid composition is controlled by water-rock interaction with igneous rock. Indications for a major magmatic contribution are lacking. Elevated B/Cl ratios observed for springs at the volcanic chain indicate a minor contribution of magmatic vapor addition. This observation is in accordance with the findings of Wrage et al. (2017), which are able to relate higher B/Cl ratios in SVZ to ATF faults misoriented to the regional stress field. The gradual transition from plutonic rocks of NPB to volcano-sedimentary rocks of the Cura-Mallín formation can be located in the volcanic chain by Sr isotopes and Rb/Sr ratios in the geothermal fluids. The geothermal circulation pattern appears to be lithology-controlled and

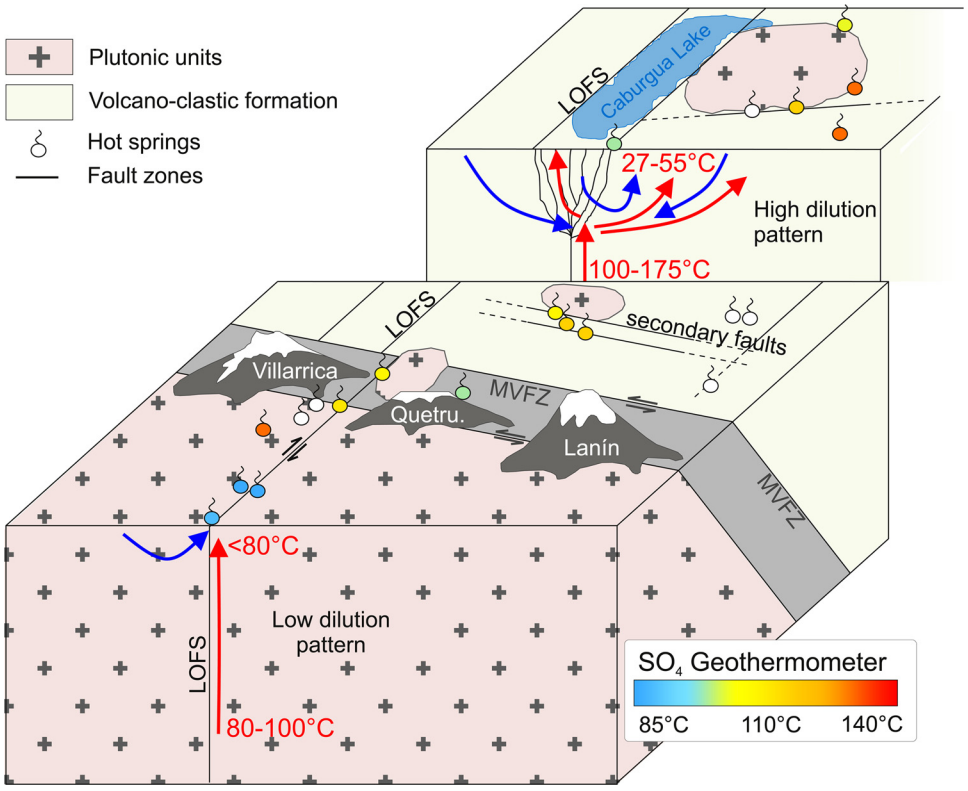

Fig. 11. Conceptual model illustrating the lithology-controlled fluid circulation proposed for the Villarrica geothermal system. Hot spring locations are marked by circular springs symbols with color code representing estimated reservoir temperature from oxygen isotope fractionation of the SO_4-H_2O system (white symbols = springs not sampled). Blue and red arrows represent the movement of meteoric and deep geothermal fluids respectively. (For interpretation of the references to colour in this figure legend, the reader is referred to the web version of this article.)

therefore showing formation-specific differences. In the plutonic sequence along the LOFS a channeled fluid flow on discrete, permeable conduits is suggested. In the Cura-Mallín formation, ramified fluid movement appears to be distributed over a wide spread fracture and fault network. Similar fluid movement conditions are suggested by Sánchez-Alfaro et al. (2016) for the Tolhuaca geothermal reservoir, also present inside the Cura-Mallín formation. The findings support the concept of Wrage et al. (2017) proposing subhorizontal flow in volcano-sedimentary units of the Cura-Mallín formation and vertical flow prevailing in plutonic units. Reservoir temperatures of 100–140 °C in the volcano-sedimentary units exceed the maximum temperatures of 80–100 °C determined for hot springs discharging from plutonic rocks. Maximum in-situ temperatures of up to 180 °C are estimated for individual hot springs on the flanks of the Villarrica volcano.

5. Conclusion

The principal goal of geothermal exploration methods is the identification of hydraulic and thermal reservoir properties. Very often, in early stages of geothermal exploration hot spring fluids are the only, yet indirect access to the subsurface allowing forecasts on geothermal reservoir conditions. The specific situation at the Villarrica-Quetrupillán-Lanín volcanic chain with numerous hot springs discharging could be used to test different geochemical methodologies. The combination of different geochemical methods (CFC, Sr isotopes, geothermometry, etc.) enables a detailed investigation on subsurface conditions regarding subsurface mixing, identification of reservoir rocks and reservoir temperatures.

Since only minor geochemical variations of rock composition are exposed, Sr isotope signatures in combination with Rb and Sr concentrations turned out to be a most sensitive lithology tracer. The lithology transition can be traced in the fluid signature and situated in the volcanic chain. Therewith the methodology can be used to exhibit the contrast between the plutonic formations south of the volcanic chain towards the volcano-sedimentary units in the north. CFC species in combination with the fractionation of oxygen isotopes quantify the fluid systems in terms of subsurface mixing processes and reservoir temperatures. The results provide key information for a geochemically-based conceptual model hinting at a disperse, rather slow circulation along a branched fault and fracture network at higher subsurface temperatures in the volcano-sedimentary sequence. In the plutonic formations, a channeled, faster flow along distinct fault zones of the LOFS at lower subsurface temperatures is derived. Thus, lithological control of the circulation pattern is indicated. Additional hydrogeological or geophysical information would be required to support the identification of optimum geothermal reservoir conditions linked to the Cura-Mallín formation.

The application of CFC analysis offers important perspectives for future geothermal resource analysis. Since effects from dilution can be quantified and eliminated, it allows for a reconstruction of the true reservoir fluid composition. Only then, trustful estimations of reservoir temperatures can be conducted minimizing the large spread of temperature estimations from classical geothermometer approaches. For the Villarrica system the re-evaluation of different solute geothermometers, conducted in the second part of the combined study (Nitschke et al., 2018), generates concordant and plausible subsurface temperatures disclosing midium-enthalpy conditions. Besides enhancement of geothermometry the true reservoir fluid composition also enables a reliable prediction of scaling and corrosion.

Acknowledgements

The study is part of a collaborative research project between the Karlsruhe Institute of Technology (KIT) and the Andean Geothermal Center of Excellence (CEGA, Fondap-Conicyt 15090013). The authors appreciate the support under the BMBF-CONICYT International Scientific Collaborative Research Program (FKZ 01DN14033/PCCI130025). Additional support under the topic “Geothermal Energy Systems” of the Helmholtz portfolio project “Geoenergy” and by EnBW Energie Baden-Württemberg AG is gratefully acknowledged. Special thanks go to our colleagues Diego Aravena, Daniele Tardani, Gabriel Perez, Elisabeth Eiche, and especially to Pablo Sánchez and Ignacio

Villalón for the support during fluid sampling and many fruitful discussions. The authors would like to thank Ilka Kleinhanns from the University of Tübingen for help in the strontium isotope measurements of the rock samples. We thank Tiziano Boschetti and an anonymous reviewer for their fruitful comments that helped a lot to improve the manuscript.

References

Adriasola, A.C., Thomson, S.N., Brix, M.R., Hervé, F., Stöckhert, B., 2005. Postmagmatic cooling and late Cenozoic denudation of the North Patagonian Batholith in the Los Lagos region of Chile, 41°–42°15′S. Int. J. Earth Sci. 95 (3), 504–528.

Awaleh, M.O., Hoch, F.B., Kadieh, I.H., Soubaneh, Y.D., Egueh, N.M., Jalludin, M., Boschetti, T., 2015. The geothermal resources of the Republic of Djibouti — I: hydrogeochemistry of the Obock coastal hot springs. J. Geochem. Explor. 152, 54–66.

Awaleh, M.O., Boschetti, T., Soubaneh, Y.D., Baudron, P., Kawalieh, A.D., Dabar, O.A., Ahmed, M.M., Ahmed, S.I., Daoud, M.A., Egueh, N.M., Mohamed, J., 2017. Geochemical study of the Sakalol-Harralol geothermal field (Republic of Djibouti): evidences of a low enthalpy aquifer between Manda-Inakir and Asal rift settings. J. Volcanol. Geotherm. Res. 331, 26–52.

Bohm, M., Lüth, S., Echtler, H., Asch, G., Bataille, K., Bruhn, C., Rietbrock, A., Wigger, P., 2002. The Southern Andes between 36°and 40°S latitude: seismicity and average seismic velocities. Tectonophysics 356 (4), 275–289.

Boschetti, T., 2013. Oxygen isotope equilibrium in sulfate–water systems: a revision of geothermometric applications in low-enthalpy systems. J. Geochem. Explor. 124, 92–100.

Cembrano, J., Lara, L.E., 2009. The link between volcanism and tectonics in the southern volcanic zone of the Chilean Andes: a review. Tectonophysics 471, 96–113.

Cembrano, J., Moreno, H., 1994. Geometria y naturaleza costrastante del volcanismo cuaternario entre los 38°y 46°S: Dominios compresionales y tensionales en un régimen transcurrente? 7th Congreso Geológico Chileno, Universidad de Conception, Conception, Chile, 240–244, Proceedings.

Cembrano, J., Hervé, F., Lavenu, A., 1996. The Liquiñe Ofqui fault zone: a long-lived intra-arc fault system in southern Chile. Tectonophysics 259, 55–66.

Charrier, R., Pinto, L., Rodríguez, M.P., 2007. Tectonostratigraphic evolution of the Andean Orogen in Chile. In: Moreno, T., Gibbons, W. (Eds.), The Geology of Chile. The Geological Society of London, pp. 21–114.

Cortecci, G., Boschetti, T., Mussi, M., Lameli, C.H., Mucchino, C., Barbieri, M., 2005. New chemical and original isotopic data on waters from El Tatio geothermal field, northern Chile. Geochem. J. 39 (6), 547–571.

Cortecci, G., 1974. Oxygen isotopic ratios of sulfate ions-water pairs as a possible geothermometer. Geothermics 3, 60–64.

Eisenlohr, T., 1997. The thermal springs of the Armutlu peninsula (NW Turkey) and their relationship to geology and tectonic. Active Tectonics of Northwestern Anatolia – The MARMARA Poly-Project 197–228.

Eppelbaum, L., Kutasov, I., Pilchin, A., 2014. Applied Geothermics.

Faure, G., 1986. Principles of Isotope Geology. Wiley, New York 589 pp.

Gardner, W.P., Susong, D.D., Solomon, D.K., Heasler, H.P., 2011. A multitracer approach for characterizing interactions between shallow groundwater and the hydrothermal system in the Norris Geyser Basin area, Yellowstone National Park. Geochem. Geophys. Geosyst. 12 (8), 1–17.

Giggenbach, W.F., 1991. Chemical techniques in geothermal exploration. In: D'Amore, F. (Ed.), Applications of Geochemistry in Geothermal Reservoir Development. UNITAR, Rome, Italy, pp. 118–144.

Graham, I.J., 1992. Strontium isotope composition of rotorua geothermal waters. Geothermics 21, 165–180.

Halas, S., Pluta, I., 2000. Empirical calibration of isotope thermometer (^{18}O ($SO4^{2?}$)–(^{18}O (H_2O) for low temperature brines. V Isotope Workshop, European Society for Isotope, Kraków. Poland Res. 68–71.

Hamza, V.M., Muñoz, M., 1996. Heat flow map of South America. Geothermics 25 (6), 599–646.

Hauser, A., 1997. Catastro y Caracterizacion de las Fuentes de Aguas Minerales y Termals de Chile, vol. 50. SERNAGEOMIN, Bol., pp. 83.

Held, S., Schill, E., Sanchez, P., Neumann, T., Emmerich, K., Morata, D., Kohl, T., 2015. Geological and tectonic settings preventing high-temperature geothermal reservoir development at Mt. Villarrica (Southern volcanic zone): clay mineralogy and sulfate-isotope geothermometry. In: Proceedings: World Geothermal Congress. Melbourne, Australia.

Held, S., Schill, E., Pavez, M., Díaz, D., Munoz, G., Morata, D., Kohl, T., 2016. Resistivity distribution from mid-crustal conductor to near-surface across the 1200 km long Liquiñe-Ofqui Fault System, southern Chile. Geophys. J. Int. 1387–1400.

Held, S., Nitschke, F., Schill, E., Morata, D., Eiche, E., Kohl, T., 2017. Hydrochemistry of the hot spring fluids of Villarrica geothermal system in the Andes of Southern Chile. GRC Trans. 41.

Hervé, F., 1976. Estudio geológico de la falla Liquñe-Reloncaví en el área de Liquiñe; antecedentes de un movimiento transcurrente (Provincia de Valdivia). Congr. Geol. Chil. Actas 1, B39–B56.

Hervé, F., 1984. Rejuvenecimientode edades radiométricas y el sistema de fallas Liquine-Ofqui. Com. Dep. Geol. Univ. Chile 35, 107–116.

Hickey-Vargas, R., Moreno-Roa, H., Lopez-Escobar, L., Frey, F., 1989. Geochemical variations in Andean basaltic and silicic lavas from the Villarrica-Lanin volcanic chain (39.5°S): an evaluation of source heterogeneity, fractional crystallization and crustal assimilation. Contrib. Mineral. Petrol. 103 (3), 361–386.

Hoering, T.C., Kennedy, J.W., 1957. The exchange of oxygen between sulfuric acid and water. J. Am. Chem. Soc. 79, 56–60.

Jacques, G., Hoernle, K., Gill, J., Wehrmann, H., Bindeman, I., Lara, L.E., 2014. Geochemical variations in the Central Southern Volcanic Zone, Chile (38–43°S): The role of fluids in generating arc magmas. Chem. Geol. 371, 27–45.

Jaupart, C., Mareschal, J.-C., Iarotsky, L., 2016. Radiogenic heat production in the continental crust. Lithos 262, 398–427.

Jordan, T.E., Burns, W.M., Veiga, R., Pángaro, F., Copeland, P., Kelly, S., Mpodozis, C., 2001. Extension and basin formation in the southern Andes caused by increased convergence rate: a mid-cenozoic trigger for the Andes. Tectonics 20 (3), 308–324.

Lara, L.E., Moreno, H., 2004. Geología del Área Liquiñe-Neltume. Carta Geológica de Chile No. 83. SERNAGEOMIN.

Lara, L.E., Lavenu, A., Cembrano, J., Rodríguez, C., 2006. Structural controls of volcanism in transversal chains: resheared faults and neotectonics in the Cordín Caulle–Puyehue area (40.5°S), Southern Andes. J. Volcanol. Geotherm. Res. 158 (1–2), 70–86.

Le Maitre, 2005. Igneous Rocks: A Classification and Glossary of Terms: Recommendation of the International Union of Geological Sciences, Subcommission on the Systematics of Igneous Rocks, 2nd ed. Cambridge Univ. Press, Cambridge 236 pp.

Lloyd, R.M., 1968. Oxygen isotope behavior in the sulfate-water system. J. Geochem. Explor. 73, 6099–6110.

Lopez-Escobar, L., Cembrano, J., Moreno, H., 1995. Geochemistry and tectonics of the Chilean southern Andes basaltic Quaternary volcanism (37–46°S). Rev. Geol. Chile 22, 219–234.

Małoszewski, P., Zuber, A., 1982. Determining the turnover time of groundwater systems with the aid of environmental tracers. J. Hydrol. 57 (3–4), 207–231.

Mc-Millan, N.J., Harmon, R.S., Moorbath, S., Lopez-Escobar, L., Strong, D.F., 1989. Crustal sources involved in continental arc magmatism: a case study of volcan Mocho-Choshuenco, southern Chile. Geology 17 (12), 1152–1156.

Meixner, J., Schill, E., Gaucher, E., Kohl, T., 2014. Inferring the in situ stress regime in deep sediments: an example from the Bruchsal geothermal site. Geotherm. Energy 2 (7).

Middlemost, E.A.K., 1994. Naming materials in the magma/igneous rock system. Earth Sci. Rev. 37 (3–4), 215–224.

Moreno, H., Lara, L.E., 2008. Geología de Área Pucón-Curarrehue. Carta Geológica de Chile No. 115. SERNAGEOMIN.

Morikawa, N., 2005. Estimation of groundwater residence time in a geologically active region by coupling ^{4}He concentration with helium isotopic ratios. Geophys. Res. Lett. 32 (2), 1–4.

Munizaga, F., Herve, F., Drake, R., Pankhurst, R.J., Brook, M., Snelling, N., 1988. Geochronology of the lake region of south-central Chile (39°–42°S): preliminary results. J. South Am. Earth Sci. 1 (3), 309–316.

NOAA, 2015. Combined Chloroflurocarbon Data from the NOAA/ESRL Global Monitoring Division.

Nitschke, F., Held, S., Villalón, I., Neumann, T., Kohl, T., 2017. Assessment of performance and parameter sensitivity of multicomponent geothermometry applied to a medium enthalpy geothermal system. Geotherm. Energy 5 (12), 1–20.

Nitschke, F., Held, S., Neumann, T., Kohl, T., 2018. Geochemical characterization of the geothermal system at Villarrica volcano, Southern Chile; Part II: site-specific Re-evaluation of SiO_2 and Na-K Solute Geothermometers. Geothermics. http://dx.doi.org/10.1016/j.geothermics.2018.03.006.

Pérez, Y., 1999. Fuentes de Aguas Termales de la Cordillera Andina del Centro-Sur de Chile (39–42°S) 54 SERNAGEOMIN, Bol. 68 pp.

Pérez-Flores, P., Cembrano, J., Sánchez-Alfaro, P., Veloso, E., Arancibia, G., Roquer, T., 2016. Tectonics, magmatism and paleo-fluid distribution in a strike-slip setting: insights from the northern termination of the Liquiée–Ofqui fault System, Chile. Tectonophysics 680, 192–210.

Pankhurst, R.J., Hervé, F., Rojas, L., Cembrano, J., 1992. Magmatism and tectonics in continental Chiloé, Chile. Tectonophysics 205, 283–294.

Pankhurst, R.J., Weaver, S.D., Hervé, F., Larrondo, P., 1999. Mesozoic – Cenozoic Evolution of the North Patagonian Batholith in Aysén Southern Chile. J. Geol. Soc. Lond. 156, 673–694.

Pearson, F.J., 1991. Applied Isotope Hydrogeology: A Case Study in Northern Switzerland. Technical Report 88-01. Distributors for the U.S. and Canada Elsevier Science Pub. Co; Elsevier New York, NY, U.S.A, Amsterdam, New York, 19 pp.

Petit-Breuilh, M.E., Lobato, J., 1994. Analisis Comparativo de la Cronologia Eruptiva Historica de los Volcanes Llaima y Villarrica (38°–39°L.S.). In: Concenption, Chile. Proceedings: 7th Congreso Geológico Chileno, Universidad de Concenption 13. pp. 366–370.

Plummer, L.N., Busenberg, E., 2006. Use of Chlorofluorocarbons in Hydrology: A Guidebook. IAEA, Vienna, Vienna 277 pp.

Radic, J.P., 2010. Las cuencas cenozoicas y su control en el volcanismo de los Complejos Nevados de Chillán y Copahue-Callaqui (Andes del Sur, 36–39°S). Andean Geol. 37 (1), 220–246.

Rowland, J.V., Sibson, R.H., 2004. Structural controls on hydrothermal flow in a segmented rift system Taupo Volcanic Zone, New Zealand. Geofluids 4, 259–283.

Rybach, L., 1976. Radioactive heat production in rocks and its relation to other petrophysical parameters. Pure Appl. Geophys. 114 (2), 309–317.

Sánchez, P., Pérez-Flores, P., Arancibia, G., Cembrano, J., Reich, M., 2013. Crustal deformation effects on the chemical evolution of geothermal systems: the intra-arc Liquiáe–Ofqui fault system, Southern Andes. Int. Geol. Rev. 55 (11), 1384–1400.

Sánchez-Alfaro, P., Reich, M., Arancibia, G., Pérez-Flores, P., Cembrano, J., Driesner, T., Lizama, M., Rowland, J., Morata, D., Heinrich, C.A., Tardani, D., Campos, E., 2016. Physical, chemical and mineralogical evolution of the Tolhuaca geothermal system, southern Andes, Chile: insights into the interplay between hydrothermal alteration and brittle deformation. J. Volcanol. Geotherm. Res. 324, 88–104.

Stern, C.R., 2004. Active Andean volcanism: its geologic and tectonic setting. Andean

Geol. 31 (2), 161–206.
Stettler, A., 1977. 87Rb-87Sr systematics of a geothermal water-rock association in the massif central, France. Earth Planet. Sci. Lett. 34, 432–438.
Stober, I., Bucher, K., 1999. Deep groundwater in the crystalline basement of the black forest region. Appl. Geochem. 14, 237–254.
Suarez, M., Emparan, C., 1995. The stratigraphy, geochronology and paleophysiography of a Miocene fresh-water interarc basin, southern Chile. J. South Amer. Earth Sci. 8 (1), 17–31.
Tardani, D., Reich, M., Roulleau, E., Takahata, N., Sano, Y., Pérez-Flores, P., Sánchez-Alfaro, P., Cembrano, J., Arancibia, G., 2016. Exploring the structural controls on helium, nitrogen and carbon isotope signatures in hydrothermal fluids along an intra-arc fault system. Geochim. Cosmochim. Acta 184, 193–211.
Turnadge, C., Smerdon, B.D., 2014. A review of methods for modelling environmental tracers in groundwater: advantages of tracer concentration simulation. J. Hydrol. 519, 3674–3689.
Villalón, I., 2015. Lithological Controls Influencing the Geochemistry of Geothermal Systems North of the Villarrica Volcano, an Experimental Approach. Santiago de Chile (B.Sc. Thesis).
Waber, H.N., Schneeberger, R., Mäder, U.K., Wanner, C., 2017. Constraints on evolution and residence time of geothermal water in granitic rocks at grimsel (Switzerland). Procedia Earth Planet. Sci. 17, 774–777.
Wrage, J., Tardani, D., Reich, M., Daniele, L., Arancibia, G., Cembrano, J., Sánchez-Alfaro, P., Morata, D., Pérez-Moreno, R., 2017. Geochemistry of thermal waters in the Southern Volcanic Zone, Chile – implications for structural controls on geothermal fluid composition. Chem. Geol. 466, 545–561.
Yokochi, R., Sturchio, N.C., Purtschert, R., Jiang, W., Lu, Z.-T., Mueller, P., Yang, G.-M., Kennedy, B.M., Kharaka, Y., 2013. Noble gas radionuclides in Yellowstone geothermal gas emissions: a reconnaissance. Chem. Geol. 339, 43–51.
Zeebe, R.E., 2010. A new value for the stable oxygen isotope fractionation between dissolved sulfate ion and water. Geochim. Cosmochim. Acta 74 (3), 818–828.
Zhonghe, P., 2001. Isotope and chemical geothermometry and its applications. Sci. China 44, 16–20.
Zoback, M.D., 2011. Reservoir Geomechanics, 5. print ed. Cambridge Univ. Press, Cambridge 449 pp.